Magnetic and transport properties of the topological compound DySbTe

Fei Gao,[1,2] Jianqi Huang,[1] Weijun Ren,[1,2,*] Mingze Li,[1] Han Wang,[1] Teng Yang,[1,2] Bing Li,[1,2] and Zhidong Zhang[1,2]
[1]*Shenyang National Laboratory for Materials Science, Institute of Metal Research, Chinese Academy of Sciences, Shenyang 110016, China*
[2]*School of Materials Science and Engineering, University of Science and Technology of China, Shenyang 110016, China*

(Received 21 February 2022; revised 16 May 2022; accepted 15 June 2022; published 27 June 2022)

We report the magnetic susceptibilities $\chi(T)$, magnetization $M(H)$, transport properties $\rho(T, H)$, and heat capacity $C_P(T)$ of DySbTe single crystal. DySbTe is an isostructural compound with the nonmagnetic Dirac nodal line (DNL) semimetal ZrSiS, in which Dy spins show a long-range antiferromagnetic (AFM) ordering below Néel temperature $T_N = 7$ K. A steplike magnetization curve and a 1/2 magnetization plateau were observed at 2 K for a magnetic field H applied parallel to the ab plane. The temperature dependence of electrical resistivity of DySbTe shows a bad-metal-like state and a peak at about 7 K associated with the AFM phase transition. The transverse magnetoresistance exhibits a crossover at a critical field from the semiclassical weak-field H^2 dependence to the high-field linear dependence, due to the Dirac nodal line states in DySbTe. The first principles calculations of band structures illustrate that DySbTe is a DNL semimetal and turns to be a weak topological insulator if the spin-orbit coupling is considered. DySbTe will be a new topological compound exhibiting the complex interplay between magnetism, topology, and electron correlations.

DOI: 10.1103/PhysRevB.105.214434

I. INTRODUCTION

Topological materials have the advantages of an ultrahigh mobility, a high magnetoresistance (MR), and a chiral anomaly [1,2], which can be used in next-generation spintronic devices, and thus have attracted great attention in quantum physics. Such materials, including topological insulators (TIs) and topological semimetals, possess topological nontrivial bulk states and/or surface states [3–9]. The former ones have an insulating state in the bulk and a gapless surface state of $E(k)$ linear dispersion showing time-reversal symmetry (TRS) or crystalline symmetry-protected massless tunneling of Dirac fermions [10], while the later ones have bulk conduction and valence bands touching at single or multiple discrete points at the Fermi level distinguished as a Dirac semimetal or Weyl semimetal [11,12]. Previous studies were mainly focused on these topological materials with discrete band crossing points [3]. When a topological material has one-dimensional continuous linear band crossing lines in the momentum space, it is called a Dirac nodal line (DNL) semimetal [11,13]. Various exotic properties such as an extremely large and anisotropic magnetoresistance [14–16], a flat optical conductivity [17], and an unconventional mass enhancement [18], may arise from the existence of DNL fermions in topological materials [19]. Recently, ZrSiS-type compounds that can be viewed as stacking of two-dimensional (2D) TIs or DNL semimetals have attracted a lot of attention [20]. It has been proven by angle-resolved photoemission spectroscope (ARPES) and first principles calculations that ZrSnTe hosts 2D electronic bands of TI state [21]. ZrSiS, ZrSiSe, and ZrSiTe have been verified as topological DNL semimetals through ARPES, transport measurement, and related calculations [3,14,16,22].

Many correlation enhancement phenomena such as charge density waves, Kondo effects, and the interplay between topological, magnetism, and electron correlations have been discovered in LnSbTe (Ln = lanthanide) compounds also crystallized in the ZrSiS-type structure. LaSbTe is considered a true nodal line semimetal with nodal line states even when spin-orbit coupling (SOC) effects are included [23,24]. When Ln is a magnetic lanthanide element, the spin degree of freedom will play an important role in material properties. CeSbTe is characterized as a low-carrier-density antiferromagnetic (AFM) Kondo lattice compound and shows magnetically tunable Weyl and Dirac states or an eightfold band cross at a high-symmetry point [25–27]. NdSbTe exhibits an AFM order with metamagnetic transitions and Kondo localization [28,29]. SmSbTe, GdSbTe, and HoSbTe are topological nodal line semimetals characterized by ARPES and first principles calculations [10,19,30–33]. These studies show that LnSbTe is a promising platform to search for new exotic topological quantum states and explore technology applications.

In this work, DySbTe single crystals were grown by the Sb flux method. The crystal structure, anisotropic magnetic susceptibilities $\chi(T)$, and magnetization $M(H)$, transport properties $\rho(T, H)$, heat capacity $C_P(T)$, and the calculated electronic band structures are reported. The results show some interesting properties, including the ordering temperature of DySbTe, the steplike magnetization curve, and a metamagnetic transition to a 1/2 magnetization plateau, bad metallic resistance behavior, and a topological nodal line semimetal or a weak topological insulator electronic band structure.

II. EXPERIMENT DETAIL

High-quality single crystals of DySbTe were grown by the Sb-flux method [34]. High-purity bulk metal Dy pieces

*wjren@imr.ac.cn

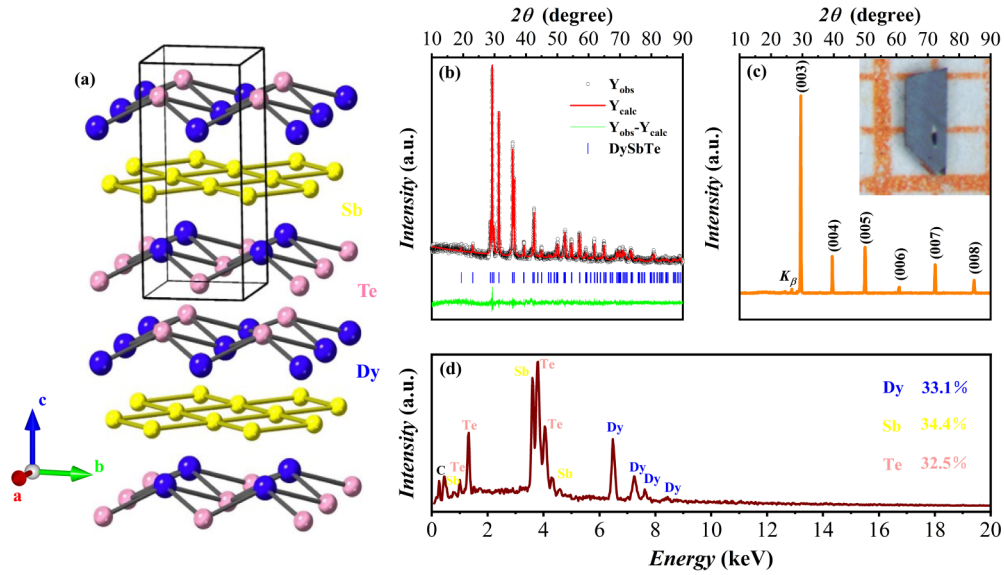

FIG. 1. (a) Crystal structure of DySbTe. (b) X-ray powder diffraction pattern of DySbTe powder (grinded from single crystals) refined with Rietveld method. (c) The XRD pattern of a flat facet for DySbTe single crystal is identified to be (001) plane of the crystal; the inset is the photograph of a typical single crystal (the back square is $1 \times 1\,\mathrm{mm}^2$). (d) The EDX spectroscopy data of the grown crystals.

(99.99%, Alfa), Te powder (99.99%, Alfa), and Sb particles (99.99%, Alfa) with a starting atomic composition of 1: 1: 30 were placed in a high-quality recrystallized alumina crucible and vacuum sealed in a quartz tube. The ampoule was heated to 1373 K over 10 h and maintained for 20 h to ensure homogeneous mixing of the starting materials. Then it was slowly cooled to 1083 K at a rate of 2 K/h, followed by centrifuging to separate the crystals from excess Sb. The obtained single crystal is in the form of flakes with metallic luster on the surface, and the size is 2 mm × 1 mm × 0.5 mm, as shown in the inset of Fig. 1(c).

A $\mathrm{Cu} - \mathrm{K}_\alpha$ x-ray diffractometer (XRD, $\lambda = 1.5418$ Å) was used for structure and composition characterization. The chemical composition of the DySbTe single crystal was analyzed using a scanning electron microscope (SEM) with an energy-dispersive x-ray spectrometer (EDX). The magnetization (M) was measured between 2 and 300 K in an applied field of 1 kOe in the field-cooling (FC) mode using a superconducting quantum interference device magnetometer (Quantum Design, Inc.). Isothermal magnetizations $M(H)$ were measured at 2–40 K with applied fields between 0 and 70 kOe of the single crystal c axis set parallel and perpendicular to the external magnetic field, respectively. The specific heat (C_P) was measured from 2 to 210 K without applied magnetic fields in a Physical Property Measurement System (PPMS, Quantum Design, Inc.). The longitudinal resistivity was measured in the PPMS with a configuration of four-wire method by silver contact.

The first principles calculations were performed within the framework of density functional theory (DFT) implemented in the QUANTUM ESPRESSO code where the projector-augmented wave (PAW) pseudopotentials were used to describe the interaction between the ion cores and the valence electrons [35,36]. Moreover, electronic exchange correlation was represented by the Perdew-Burke-Ernzerhof (PBE) functional in the generalized gradient approximation (GGA). A set of fully relativistic pseudopotentials were used for the spin-orbit coupling (SOC) case. Since the $4f$ states of the Dy element are far from the Fermi level, the magnetism was ignored throughout the calculations. To get the optimized structure, the convergence criteria for residual stress and force were set to 1×10^{-2} kbar and 1×10^{-5} Ry/bohr, respectively. The cutoff energy for the plane-wave basis was set to 80 Ry. A sufficiently dense k-point mesh of $11 \times 11 \times 5$ was adopted to numerically integrate the Hamiltonian over the first Brillouin zone. After structural relaxation, the electronic band structures with and without SOC were obtained based on the relevant ground-state charge densities.

III. RESULTS AND DISCUSSION

DySbTe crystallizes in a tetragonal structure of *P*4/*nmm* (no. 129) space group, as shown in Fig. 1(a), which is identical to the fully explored prototype topological nodal line semimetal ZrSiS [14–18]. It consists of stacking Te-Dy-Sb-Dy-Te slabs along the c axis, with Sb plane sandwiched by Dy-Te layers. The Sb planar layer is similar to the Si square net in ZrSiS that hosts 2D/quasi-2D relativistic fermions [20,37]. In this space group, the Sb atom occupies the Wyckoff position 2*b* (1/4, 3/4, 1/2) while Dy and Te occupy 2*c* (3/4, 3/4, z) site. Powder x-ray diffraction (XRD) data were collected at 300 K on crushed single crystals of DySbTe, as shown in Fig. 1(b). The refinement result of the XRD pattern reveals the single-phase nature of the crystal, representing a high crystalline quality. The refined lattice parameters are $a = b = 4.240$ Å and $c = 9.168$ Å, both smaller than the corresponding parameters for CeSbTe, SmSbTe, or GdSbTe [10,23,25,28,31]. The atomic percentages of DySbTe are Dy, Sb, Te = 33.1, 34.4, 32.5, almost perfect stoichiometry Dy : Sb : Te = 1 : 1 : 1, obtained by the EDX spectroscopy, as shown in Fig. 1(d). The XRD pattern of the big facet with a flat surface for DySbTe crystal at room temperature was

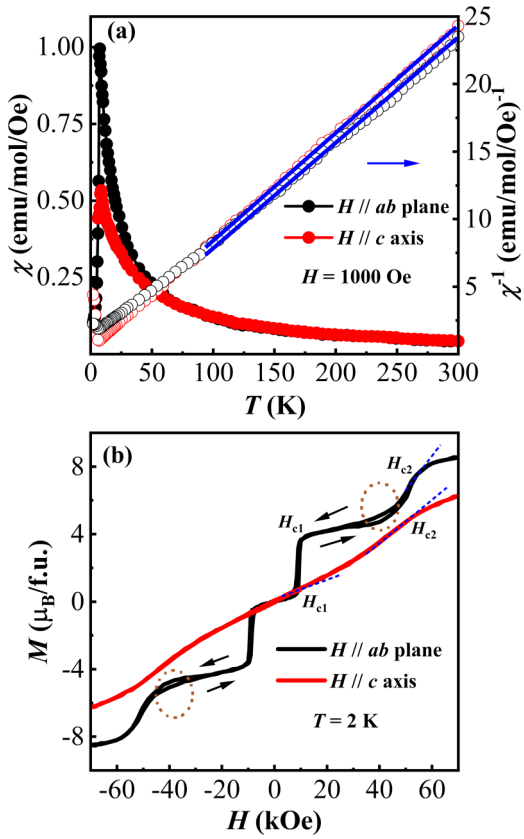

FIG. 2. (a) Magnetic susceptibility (left ordinate) of DySbTe measured in an external magnetic field of $H = 1$ kOe applied parallel and perpendicular to the crystallographic c axis and the temperature dependences of inverse susceptibility χ^{-1} and the fit to the Curie-Weiss law (right ordinate). (b) Isothermal magnetizations in −70 to 70 kOe for DySbTe single crystal at 2 K. H_{c1} and H_{c2} represent the critical fields. The brown ellipses mark the tiny hysteresis.

represented in Fig. 1(c). Only sharp (00l) peaks can be observed, indicating a uniform c axis orientation perpendicular to the facet of the single crystal.

The temperature dependence of magnetic susceptibility ($\chi^{-1} = \frac{H}{M}$) and inverse magnetic susceptibility $1/\chi$ for a magnetic field $H = 1$ kOe for H // ab plane and for H // c axis of the DySbTe single crystal are shown in Fig. 2(a). Both χ_{ab} and χ_c exhibit a distinct λ-shape peak at 7 K due to the magnetic ordering temperature T_N. The magnetic anisotropy (the difference of χ_{ab} and χ_c) decreases with increasing temperature, existing untill about 50 K, much higher than $T_N \sim 7$ K. The temperature dependencies of susceptibility above 100 K can be well fitted by the modified Curie-Weiss law $\chi = \chi_0 + \frac{C}{(T-\theta_W)}$, where χ_0 is a temperature-independent component, C is the Curie constant, and θ_w is the Curie-Weiss temperature, respectively. A θ_w of −15 K was obtained for H // ab plane and −28 K for H // c axis, revealing antiferromagnetic interactions between the magnetic moments of Dy^{3+}. The effective magnetic moments were determined to be 10.84 μ_B/f.u. for H // ab plane and 10.20 μ_B/f.u. for H // c axis, which are close to the theoretical value for Dy^{3+} ion: $\mu_{\text{eff}} = g_J\sqrt{J(J+1)}\mu_B = 10.65\,\mu_B$, with $J = 15/2$, $g_J = 4/3$.

The $M(H)$ isotherms were measured at 2 K for H up to ±70 kOe and shown in Fig. 2(b). In the low magnetic field region (−10 kOe < H < 10 kOe), $M(H)$ is linear due to the AFM ground state. With increasing magnetic field up to ∼±70 kOe for both directions, $M(H)$ increases nonlinearly. M exhibits a steeper increase with field above $H_{c1} \approx \pm 10$ kOe and evolves toward sublinear field dependence at the higher field above $H_{c2} \approx \pm 54$ kOe. The critical fields H_{c1} and H_{c2} for metamagnetic transitions are isotropy, almost the same for H // c axis and H // ab plane. There are some different behaviors for magnetization processes along two crystallographic directions. For H // c axis, the saturated field of magnetization is about ±70 kOe. The entire magnetization phenomenon can be described as an AFM to canted magnetic state transition at H_{c1} and a subsequent field-driven FM polarization at H_{c2}. Similar metamagnetic transitions were also observed in CeSbTe, NdSbTe, and GdSbTe with the AFM ground states [10,25,29]. The metamagnetic transitions and FM polarizations provide a different approach to turn on/off the time-reversal symmetry, which has been proposed to modify the topological phases in CeSbTe [25,26]. By contrast, for the H//ab plane, there is a noticeable jump of the magnetization at ±10 kOe to a value 4.2 μ_B, which is almost 1/2 of the saturation magnetization M_0. This behavior implies that the Dy moment lies along the ab plane and an average ferromagnetic component along the ab plane in the zero-field magnetic structure speculated from the low field jump. The 1/2 plateau suggests that in a unit cell of four spins along the ab plane, it could consist of three pointing in the same direction and one pointing in the opposite direction in each tetrahedron. The proposed magnetic structure would consist of the ferromagnetic planes with moments along ab plane in an "up-up-up-down" sequence. It has been reported that stabilizing the 1/2-plateau state over an extended field range is probably involving a spin-lattice coupling [38]. A tiny hysteresis in $M(H)$ marked by a "brown ellipse" can be observed for H // ab plane, indicating the first ordering attribution of the field-induced metamagnetic transition. The $M(H)$ curve shows a saturation trend in the highest available field of 70 kOe and the saturation magnetization value is $M_0 \sim 8.6\,\mu_B$, which is lower than the theoretical value of $g_J J \mu_B = 10\mu_B$ for the moment of a free Dy^{3+} ion, which may result from the crystal field effect [25].

Figures 3(a) and 3(d) represent the temperature dependence of the field-cooling (FC) magnetization M with H = 5–70 kOe measured in the field for H // ab plane and for H // c axis. On the whole, the AFM peak generally shifts to low temperature as magnetic field increases [see Figs. 3(a) and 3(d)]. To further probe the magnetic order, isothermal magnetizations were represented in Figs. 3(b) and 3(e). At temperature above T_N, the magnetization curves show linear behavior and small magnetization values, which is consistent with the paramagnetic (PM) feature. The magnetic phase diagrams inferred from the contour plots of dM/dH along two crystallographic directions are illustrated in Figs. 3(c) and 3(f). Magnetic phase diagrams contain paramagnetic phase, antiferromagnetic phase, ferromagnetic phase, and canted magnetic phase regions for H // ab plane, and paramagnetic phase, antiferromagnetic phase, and canted magnetic phase regions for H // c axis. The obtained magnetic phase diagrams

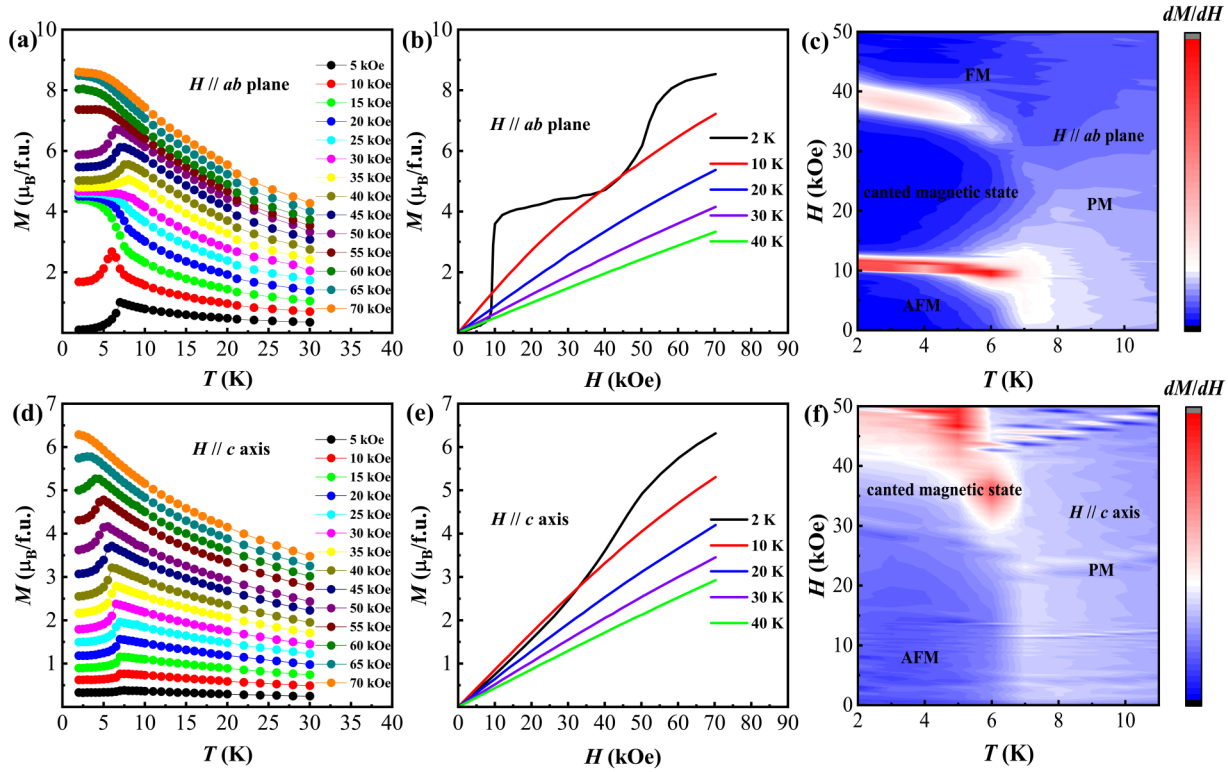

FIG. 3. Temperature dependence of the FC magnetization M with $H = 5$–70 kOe measured in the field for (a) H // ab plane and for (d) H // c axis. Magnetization (M) plotted as a function of magnetic field H of DySbTe for (b) H //ab plane and (e) H //c axis in the temperature range 2–40 K. Magnetic phase diagrams of DySbTe for H // ab plane (c) and H // c axis (f), respectively. The color maps represent dM/dH in the parameter spaces of temperature (T) and magnetic field (H).

are in good agreement with the changes of $M(T)$ curves under various magnetic fields.

In this part, we studied the correlation between magnetism and transport properties. Temperature dependence of resistivity $\rho(T)$ curves measured at various applied fields for H // c axis are represented in Fig. 4(a). With the temperature decreasing, ρ increases and then decreases, showing a broad humplike feature, where the sample is in the PM phase. This phenomenon is unusual in ZrSiS-type series materials but has been reported in HoSbTe [33]. On further cooling, ρ decreases until a significant drop near 7 K, corresponding to the PM to AFM phase transition. When magnetic fields are applied, ρ increases with increasing magnetic fields, presenting a positive magnetoresistance. An enlarged view of ρ below 10 K is shown in the inset of Fig. 4(a). The peak slightly shifts to lower temperatures with increasing of field, which is consistent with the variation of T_N in the $M(T)$ curve for H // c axis. The magnetoresistance $\mathrm{MR}(\%) = [\rho(H = 70\,\mathrm{kOe}) - \rho(H = 0)]/\rho(H = 0)$ is 26.2% at 2 K and 24.5% at 10 K respectively for an applied magnetic field of 70 kOe. At both 2 and 10 K, the curves of MR(H) are quite consistent with that of $M(H)$ for H // c axis. The MR(H) data show a crossover from the low-field H^2 dependence to the high-field linear dependence, which is often observed in Dirac materials [39–41]. Although the amount of magneto-transport data is not sufficient, it is still going some way towards indicating the existence of Dirac nodal line states in DySbTe.

The specific heat capacity (C_P) of DySbTe with zero magnetic field is shown in Fig. 5(a). The C_P decreases monotonically down to 10 K and exhibits a λ-shaped peak at about 7 K, in agreement with the observations in the magnetic susceptibility and resistivity. The inset in Fig. 5(a) shows the low-temperature C_P/T vs T^2 plots measured without a magnetic field. Assuming that the magnetic contribution is negligible when $T > T_N$, the C_P/T vs T^2 data from 9 to 18 K were fitted by the Fermi-liquid model using the expression $C/T = \gamma + \beta T^2$ [42], where γ is the electronic coefficient and β is the phonon coefficient of the heat capacity, respectively. The fit yielded $\gamma = 0.45\,\mathrm{J/mol\,K^2}$ and $\beta = 5.79 \times 10^{-4}\,\mathrm{J/mol\,K^4}$. The Debye temperature estimated from β using the relation $\theta_D = \sqrt[3]{12\pi^4 rR5/\beta}$ (where $r = 3$ is the number of atoms in the formula unit and R is the gas constant equal to 8.314 J/mol K) is 216 K. We can calculate the magnetic entropy $S_m = \int_0^T \frac{C_m(T)}{T} dT$ by subtracting the contribution of electron and phonon terms [see the inset in Fig. 5(b)]. The S_m increases with increasing temperature and reaches a saturation value of 6.65 J/mol K, which is slightly higher than $R\ln 2$ but far below the theoretical value of 23.05 J/mol K calculated from $S_m = R\ln(2J + 1)$. The low magnetic entropy of this compound originates from the doublet ground state of Dy^{3+}, since the CEF splits the 16-fold degenerate multiplet of Dy^{3+} into eight doublet states [43]. The magnetic entropy value should be closer to $R\ln 2$ instead of $R\ln 16$. Other Dy-contained compounds such as α-$DyGa_3$ also have a magnetic entropy close to $R\ln 2$ [44].

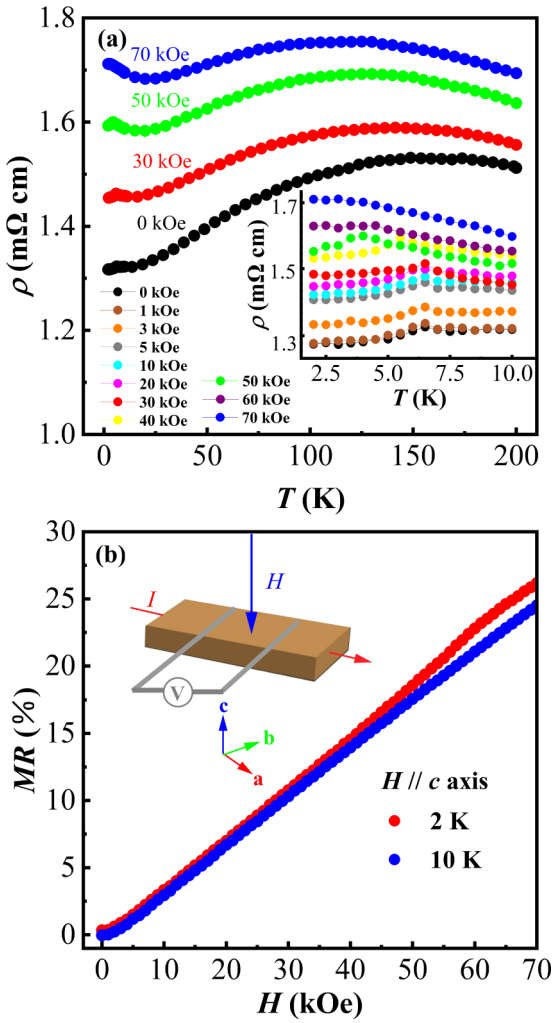

FIG. 4. (a) Resistivity ρ plotted as a function of temperature T at various applied fields for H // c axis. The inset is an enlarged view below 10 K at various applied fields. (b) Field dependence MR at 2 and 10 K of DySbTe.

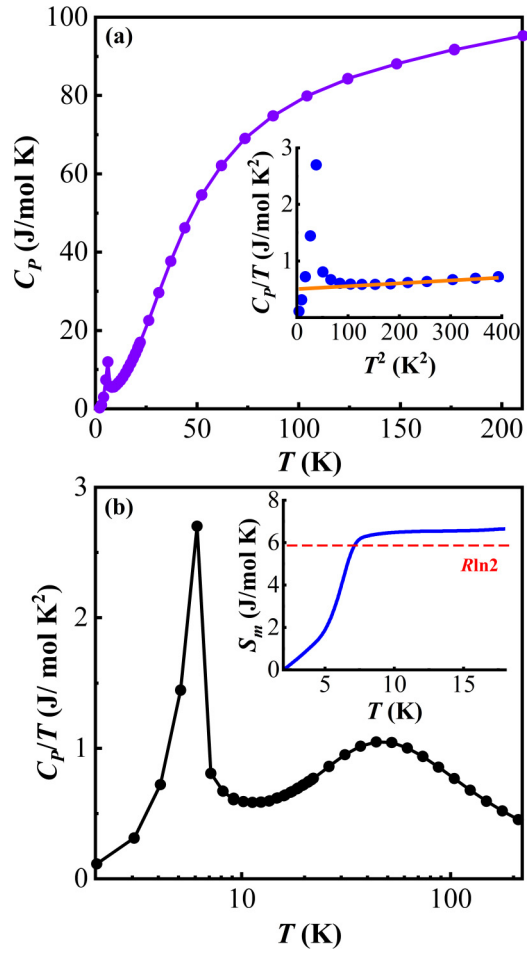

FIG. 5. (a) The specific heat capacity measured without an applied magnetic field for H // c axis. The inset shows the C_P/T-T^2 plots at low temperature. The orange solid line is a fit to the data using the Fermi-liquid model as described in the text. (b) C_P/T-T plots and the inset shows the magnetic entropy as a function of temperature.

The calculated band structures of DySbTe are shown in Fig. 6. When SOC is not taken into consideration, the calculated electronic band structures of DySbTe without and with the $4f$ electron states of Dy atoms taken into account are shown in Figs. 6(a) and 6(b), respectively. For the strongly correlated $4f$ electrons which contribute to local magnetic moments, we follow the theoretical and experimental estimates of Coulomb repulsion U for the rare earths [45] and take an on-site $U = 6$ eV in the calculation. From Fig. 6(a), the lowest conduction band and the highest valence band cross and form four distinct point-contact nodes, i.e., Dirac nodal points on the lines of symmetry directed along Γ-X, M-Γ, Z-R, and A-Z, which are actually a part of the nodal lines as shown in Figs. 6(c) and 6(d). The orbital projected band structure shows that the bands close to the Fermi level, especially around the Dirac nodal points, are dominated by p_x and p_y orbitals of Sb atoms. From Fig. 6(b), the Dy-$4f$ related bands appear at least 1 eV above the Fermi level and have no significant entanglement with the Dirac nodal line states. The dispersionless band's feature indicates that the $4f$ electrons of Dy atoms are highly localized. Moreover, the band splitting of the Dirac nodal line states (dominantly from the Sb layer) around the Fermi level between majority and minority spins is negligible indicating that the topological properties of DySbTe are marginally affected by magnetism, which is different from the case in Co_2MnGa where the nodal line states are relevant to the magnetic d orbital of Mn atoms. If magnetism were off, the band structure of Co_2MnGa would become completely different and the line nodes would disappear, showing that magnetism is essential for the topological phase of Co_2MnGa [46].

With SOC considered, we recalculate the band structure of DySbTe while safely neglecting the background magnetism due to the unpaired $4f$ electrons as analyzed above. As a matter of fact, the same treatment was also adopted in the study of other similar nodal line semimetals [19,33,47]. The SOC induces gaps in the Dirac nodal points, as shown in Fig. 6(e), and DySbTe becomes a weak topological insulator (WTI) with a symmetry-based indicator $Z_{2,2,2,4} = (0010)$, which is similar to the case of HoSbTe [33]. Figures 6(f)–6(i) give the calculated values of SOC gaps varying from 21 meV along

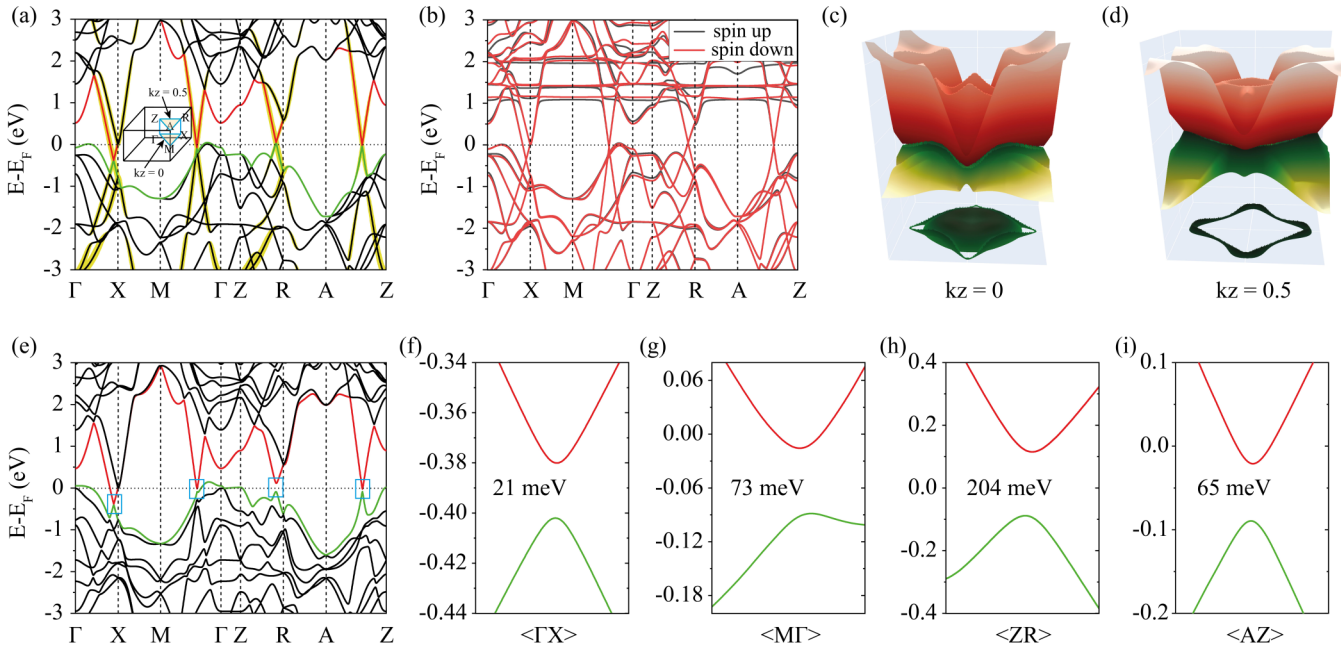

FIG. 6. (a) The calculated electronic band structures of DySbTe without f orbital of Dy atoms. The red and green lines show respectively the bottom conduction band and top valence band, and the yellow lines with varying thickness represent the weight of p_x and p_y orbitals of Sb. The inset is 3D Brillouin zone (BZ) of DySbTe. Blue lines indicate an irreducible BZ with all the high-symmetry points (Γ, X, M, Z, R, A) included. Two planes $k_z = 0$ and $k_z = 0.5$ used in (c) and (d) are defined by Γ-X-M and Z-R-A, respectively. (b) The calculated electronic band structures of DySbTe with f orbital of Dy atoms involved. Black and red lines represent spin up and spin down bands, respectively. (c),(d) Dirac nodal lines comprised of states in the $k_z = 0$ plane and $k_z = 0.5$ plane, respectively. The bottom panels clearly show the loop shape of the nodal lines in the top valence band. (e) The calculated electronic band structure of DySbTe with SOC. Blue rectangle indicates the SOC-induced band gaps at the Dirac nodal points. (f)–(i) the zoomed-in SOC gaps along the high-symmetry directions of Γ-X, M-Γ, Z-R, and A-Z, respectively, with the gap values given in each panel.

Γ-X to 204 meV along Z-R, all of which show much larger SOC strength than that (<1 meV) in the magnetism-induced nodal lines in Co_2MnGa [48].

IV. CONCLUSION

We have grown a magnetic DySbTe single crystal with ZrSiS-type structure using the self-flux method. The crystal structure refinement of DySbTe confirms the noncentrosymmetric tetragonal symmetry of space group P_4/nmm being identical to the nonmagnetic topological nodal line semimetal ZrSiS system. $\chi(T)$ and $C_P(T)$ study results reveal AFM transition at $T_N \sim 7$ K. Meanwhile, DySbTe exhibits a large anisotropic magnetic property at low temperatures. The MR(H) exhibits a weak-field H^2 dependence to the high-field linear dependence, indicating the existence of Dirac nodal line states in DySbTe. Our first principles calculations of electronic band structures for DySbTe show a topological nodal line semimetal or a weak topological insulator without or with considering the effect of SOC. This material provides an ideal platform for investigating the interplay between magnetism, topological, and electron correlation physics in topological quantum materials.

ACKNOWLEDGMENTS

This work has been supported by the Ministry of Science and Technology of China (Grant No. 2021YFB3501201) and the National Natural Science Foundation of China (Grant No. 52071323).

[1] H. Li, H. He, H.-Z. Lu, H. Zhang, H. Liu, R. Ma, Z. Fan, S.-Q. Shen, and J. Wang, Negative magnetoresistance in Dirac semimetal Cd_3As_2, Nat. Commun. **7**, 10301 (2016).

[2] J. Xiong, S. K. Kushwaha, T. Liang, J. W. Krizan, M. Hirschberger, W. Wang, R. J. Cava, and N. P. Ong, Evidence for the chiral anomaly in the Dirac semimetal Na_3Bi, Science **350**, 413 (2015).

[3] S. W. Xue, M. Y. Wang, Y. Li, S. Y. Zhang, X. Jia, J. H. Zhou, Y. G. Shi, X. T. Zhu, Y. G. Yao, and J. D. Guo, Observation of Nodal-Line Plasmons in ZrSiS, Phys. Rev. Lett. **127**, 186802 (2021).

[4] M. Z. Hasan and C. L. Kane, Colloquium: Topological insulators, Rev. Mod. Phys. **82**, 3045 (2010).

[5] X.-L. Qi and S.-C. Zhang, Topological insulators and superconductors, Rev. Mod. Phys. **83**, 1057 (2011).

[6] B. Yan and C. Felser, Topological materials: Weyl semimetals, Annu. Rev. Condens. Matter Phys. **8**, 337 (2017).

[7] N. P. Armitage, E. J. Mele, and A. Vishwanath, Weyl and Dirac semimetals in three-dimensional solids, Rev. Mod. Phys. **90**, 015001 (2018).

[8] H. Gao, J. W. Venderbos, Y. Kim, and A. M. Rappe, Topological semimetals from first principles, Annu. Rev. Mater. Res. **49**, 153 (2019).

[9] X. Chen, J. Liu, and J. Li, Topological phononic materials: Computation and data, Innovation **2**, 100134 (2021).

[10] R. Sankar, I. P. Muthuselvam, K. R. Babu, G. S. Murugan, K. Rajagopal, R. Kumar, T.-C. Wu, C.-Y. Wen, W.-L. Lee, G.-Y. Guo, and F.-C. Chou, Crystal growth and magnetic properties of topological nodal-line semimetal GdSbTe with antiferromagnetic spin ordering, Inorg. Chem. **58**, 11730 (2019).

[11] A. A. Burkov, M. D. Hook, and L. Balents, Topological nodal semimetals, Phys. Rev. B **84**, 235126 (2011).

[12] F. Arnold, C. Shekhar, S.-C. Wu, Y. Sun, R. Donizeth dos Reis, N. Kumar, M. Naumann, M. O. Ajeesh, M. Schmidt, A. G. Grushin, J. H. Bardarson, M. Baenitz, D. Sokolov, H. Borrmann, M. Nicklas, C. Felser, E. Hassinger, and B. Yan, Negative magnetoresistance without well-defined chirality in the Weyl semimetal TaP, Nat. Commun. **7**, 11615 (2016).

[13] C. Fang, Y. Chen, H.-Y. Kee, and L. Fu, Topological nodal line semimetals with and without spin-orbital coupling, Phys. Rev. B **92**, 081201(R) (2015).

[14] M. N. Ali, L. M. Schoop, C. Garg, J. M. Lippmann, E. Lara, B. Lotsch, and S. S. P. Parkin, Butterfly magnetoresistance, quasi-2D Dirac fermi surface and topological phase transition in ZrSiS, Sci. Adv. **2**, e1601742 (2016).

[15] Y.-Y. Lv, B.-B. Zhang, X. Li, S.-H. Yao, Y. B. Chen, J. Zhou, S.-T. Zhang, M.-H. Lu, and Y.-F. Chen, Extremely large and significantly anisotropic magnetoresistance in ZrSiS single crystals, Appl. Phys. Lett. **108**, 244101 (2016).

[16] R. Singha, A. K. Pariari, B. Satpati, and P. Mandal, Large nonsaturating magnetoresistance and signature of nondegenerate Dirac nodes in ZrSiS, Proc. Natl. Acad. Sci. USA. **114**, 2468 (2017).

[17] M. B. Schilling, L. M. Schoop, B. V. Lotsch, M. Dressel, and A. V. Pronin, Flat Optical Conductivity in ZrSiS Due to Two-Dimensional Dirac Bands, Phys. Rev. Lett. **119**, 187401 (2017).

[18] S. Pezzini, M. R. van Delft, L. M. Schoop, B. V. Lotsch, A. Carrington, M. I. Katsnelson, N. E. Hussey, and S. Wiedmann, Unconventional mass enhancement around the Dirac nodal loop in ZrSiS, Nat. Phys. **14**, 178 (2018).

[19] S. S. Yue, Y. T. Qian, M. Yang, D. Y. Geng, C. J. Yi, S. Kumar, K. Shimada, P. Cheng, L. Chen, Z. J. Wang, H. M. Weng, Y. G. Shi, K. H. Wu, and B. J. Feng, Topological electronic structure in the antiferromagnet HoSbTe, Phys. Rev. B **102**, 155109 (2020).

[20] Q. N. Xu, Z. D. Song, S. M. Nie, H. M. Weng, Z. Fang, and X. Dai, Two-dimensional oxide topological insulator with iron-pnictide superconductor lifeas structure, Phys. Rev. B **92**, 205310 (2015).

[21] R. Lou, J.-Z. Ma, Q.-N. Xu, B.-B. Fu, L.-Y. Kong, Y.-G. Shi, P. Richard, H.-M. Weng, Z. Fang, S.-S. Sun, Q. Wang, H.-C. Lei, T. Qian, H. Ding, and S.-C. Wang, Emergence of topological bands on the surface of ZrSnTe crystals, Phys. Rev. B **93**, 241104(R) (2016).

[22] B. B. Fu, C.-J. Yi, T.-T. Zhang, M. Caputo, J.-Z. Ma, X. Gao, B. Q. Lv, L.-Y. Kong, Y.-B. Huang, P. Richard, M. Shi, V. N. Strocov, C. Fang, H.-M. Weng, Y.-G. Shi, T. Qian, and H. Ding, Dirac nodal surfaces and nodal lines in ZrSiS, Sci. Adv. **5**, eaau6459 (2019).

[23] R. Singha, A. Pariari, B. Satpati, and P. Mandal, Magnetotransport properties and evidence of a topological insulating state in LaSbTe, Phys. Rev. B **96**, 245138 (2017).

[24] Y. Wang, Y. Qian, M. Yang, H. X. Chen, C. Li, Z. Y. Tan, Y. Q. Cai, W. J. Zhao, S. Y. Gao, Y. Feng, S. Kumar, E. F. Schwier, L. Zhao, H. M. Weng, Y. G. Shi, G. Wang, Y. T. Song, Y. B. Huang, K. Shimada, Z. Y. Xu, X. J. Zhou, and G. D. Liu, Spectroscopic evidence for the realization of a genuine topological nodal-line semimetal in LaSbTe, Phys. Rev. B **103**, 125131 (2021).

[25] B. J. Lv, J. Chen, L. Qiao, J. Ma, X. Yang, M. Li, M. Wang, Q. Tao, and Z.-A. Xv, Magnetic and transport properties of low-carrier-density kondon semimetal CeSbTe, J. Phys.: Condens. Matter **31**, 355601 (2019).

[26] L. M. Schoop, A. Topp, J. Lippmann, F. Orlandi, L. Müchler, M. G. Vergniory, Y. Sun, A. W. Rost, V. Duppel, M. Krivenkov, S. Sheoran, P. Manuel, A. Varykhalov, B. Yan, R. K. Kremer, C. R. Ast, and B. V. Lotsch, Tunable Weyl and Dirac states in the nonsymmorphic compound CeSbTe, Sci. Adv. **4**, eaar2317 (2018).

[27] A. Weiland, D. G. Chaparro, M. G. Vergniory, E. Derunova, J. Yoon, I. W. H. Oswalad, G. T. McCandless, M. Ali, and J. Y. Chan, Band structure engineering of chemically tunable LnSbTe (Ln = La, Ce, Pr), APL Mater. **7**, 101113 (2019).

[28] R. Sankar, I. P. Muthuselvam, K. Rajagopal, K. R. Babu, G. S. Murugan, K. S. Bayikadi, K. Moovendaran, C. T. Wu, and G.-Y. Guo, Anisotropic magnetic properties of nonsymmorphic semimetallic single crystal NdSbTe, Cryst. Growth Des. **20**, 6585 (2020).

[29] K. Pandey, R. Basnet, A. Wegner, G. Acharya, M. R. Un Nabi, J. Liu, J. Wang, Y. K. Takahashi, B. Da, and J. Hu, Electronic and magnetic properties of the topological semimetal candidate NdSbTe, Phys. Rev. B **101**, 235161 (2020).

[30] M. N. Hosen, K. Dhakal, P. Maldonado, A. Aperis, F. Kabir, C. Sims, P. Riseborough, P. M. Oppeneer, D. Kaczorowski, T. Durakiewicz, and M. Neupane, Discovery of topological nodalline fermionic phase in a magnetic material GdSbTe, Sci. Rep. **8**, 13283 (2018).

[31] K. Pandey, D. Mondal, J. W. Villanova, J. Roll, R. Basnet, A. Wegner, G. Acharya, M. R. U. Nabi, B. Ghosh, J. Fujii, J. Wang, B. Da, A. Agarwal, I. Vobornik, A. Politano, S. Barraza-Lopez, and J. Hu, Magnetic topological semimetal phase with electronic correlation enhancement in SmSbTe, Adv. Quantum Technol. **4**, 2100063 (2021).

[32] S. Regmi, G. Dhakal, F. C. Kabeer, N. Harrison, F. Kabir, A. P. Sakhya, K. Gofryk, D. Kaczorowski, P. M. Oppeneer, and M. Neupane, Observation of multiple nodal-lines in SmSbTe, Phys. Rev. Materials **6**, L031201 (2022).

[33] M. Yang, Y. T. Qian, D. Y. Yan, Y. Li, Y. T. Song, Z. J. Wang, C. J. Yi, H. L. Feng, H. M. Weng, and Y. G. Shi, Magnetic and electronic properties of a topological nodal line semimetal candidate: HoSbTe, Phys. Rev. Materials **4**, 094203 (2020).

[34] P. C. Canfield and Z. Fisk, Growth of single crystals from metallic fluxes, Philos. Mag. **65**, 1117 (1992).

[35] P. Giannozzi, S. Baroni, N. Bonini, M. Calandra, R. Car, C. Cavazzoni, D. Ceresoli, G. L. Chiarotti, M. Cococcioni, I. Dabo, A. D. Corso, S. d. Gironcoli, S. Fabris, G. Fratesi, R. Gebauer, U. Gerstmann, C. Gougoussis, A. Kokalj, M. Lazzeri, L. Paulatto *et al.*, Quantum ESPRESSO: A modular andopen-

source software project for quantum simulations of materials, J. Phys.: Condens. Matter **21**, 395502 (2009).

[36] P. Giannozzi, O. Andreussi, T. Brumme, O. Bunau, M. B. Nardelli, M. Calandra, R. Car, C. Cavazzoni, D. Ceresoli, and M. Cococcioni, Advanced capabilities for materials modelling with quantum ESPRESSO, J. Phys.: Condens. Matter **29**, 465901 (2017).

[37] M. Neupane, I. Belopolski, M. M. Hosen, D. S. Sanchez, R. Sankar, M. Szlawska, S.-Y. Xu, K. Dimitri, N. Dhakal, P. Maldonado, P. M. Oppeneer, D. Kaczorowski, F. Chou, M. Z. Hasan, and T. Durakiewicz, Observation of topological nodal fermion semimetal phase in ZrSiS, Phys. Rev. B **93**, 201104(R) (2016).

[38] C. Lacroix, P. Mendels, and F. Mila, *Introduction to Frustrated Magnetism* (Springer, Berlin, 2011).

[39] A. F. Wang, D. Graf, A. Stein, Y. Liu, W. G. Yin, and C. Petrovic, Magnetotransport properties of MoP_2, Phys. Rev. B **96**, 195107 (2017).

[40] W. J. Ren, A. F. Wang, D. Graf, Y. Liu, Z. D. Zhang, W.-G. Yin, and C. Petrovic, Absence of Dirac states in $BaZnBi_2$ induced by spin-orbit coupling, Phys. Rev. B **97**, 035147 (2018).

[41] J. Y. Liu, P. F. Liu, K. Gordon, E. Emmanouilidou, J. Xing, D. Graf, B. C. Chakoumakos, Y. Wu, H. B. Cao, D. Dessau, Q. H. Liu, and N. Ni, Nontrivial topology in the layered Dirac nodal-line semimetal candidate $SrZnSb_2$ with distorted Sb square nets, Phys. Rev. B **100**, 195123 (2019).

[42] K.-W. Chen, Y. Lai, Y.-C. Chiu, S. Steven, T. Besara, D. Graf, T. Siegrist, T. E. Albrecht-Schmitt, L. Balicas, and R. E. Baumbach, Possible devil's staircase in the kondo lattice CeSbSe, Phys. Rev. B **96**, 014421 (2017).

[43] L. S. Wu, S. E. Nikitin, M. Frontzek, A. I. Kolesnikov, G. Ehlers, M. D. Lumsden, K. A. Shaykhutdinov, E.-J. Guo, A. T. Savici, Z. Gai, A. S. Sefat, and A. Podlesnyak, Magnetic ground state of the Ising-like antiferromagnet $DyScO_3$, Phys. Rev. B **96**, 144407 (2017).

[44] M.-R. Cong, C.-W. Wang, W.-J. Ren, M. Avdeev, C. D. Ling, F. Gao, B. Li, and Z.-D. Zhang, Magnetic ordering in the rhombohedral α-$DyGa_3$, J. Alloy. Compd. **903**, 163906 (2022).

[45] J. F. Herbst, R. E. Watson, and J. W. Wilkins, Relativistic calculations of $4f$ excitation energies in the rare-earth metals: Further results, Phys. Rev. B **17**, 3089 (1978).

[46] I. Belopolski, K. Manna, D. S. Sanchez, G. Q. Chang, B. Ernst, J. X. Yin, S. T. S. Zhang, T. Cochran, N. Shumiya, H. Zheng, B. Singh, G. Bian, D. Multer, M. Litskevich, X. T. Zhou, S.-M. Huang, B. K. Wang, T.-R. Chang, S.-Y. Xu, A. Bansil, C. Felser, H. Lin, and M. Z. Hasan, Discovery of topological Weyl fermion lines and drumhead surface states in a room temperature magnet, Science **365**, 1278 (2019).

[47] A. Topp, M. G. Vergniory, M. Krivenkov, A. Varykhalov, F. Rodolakis, J. L. McChesney, B. V. Lotsch, C. R. Ast, and L. M. Schoop, The effect of spin-orbit coupling on nonsymmorphic square-net compounds, J. Phys. Chem. Solids **128**, 296 (2019).

[48] G. Q. Chang, S.-Y. Xu, X. T. Zhou, S.-M. Huang, B. Singh, B. K. Wang, I. Belopolski, J. X. Yin, S. T. Zhang, A. Bansil, H. Lin, and M. Z. Hasan, Topological Hopf and Chain Link Semimetal States and Their Application to Co_2MnGa, Phys. Rev. Lett. **119**, 156401 (2017).